

# A cost-effective method for producing spatially continuous high-resolution air temperature information in urban environments



Umer Alvi <sup>\*</sup>, Juuso Suomi, Jukka Käyhkö

Section of Geography, Department of Geography and Geology, University of Turku, Turku, Finland

## ARTICLE INFO

**Keywords:**

Spatial temperature variation  
Air temperature modeling  
Land surface temperature  
Landsat 8  
CORINE land cover  
Emissivity

## ABSTRACT

Sustainable city planning requires detailed information on spatial temperature variations. Remotely sensed land surface temperature (LST) is known to differ substantially from air temperature (AT) causing misinterpretations of the ambient conditions. We demonstrate a reliable and cost-efficient method for AT modelling in urban environments using open data and few temperature observations. The study area is the city of Turku SW Finland, where we have a dense in situ AT observation network of 64 Onset Hobo temperature loggers as a reference. Landsat 8 thermal data from different seasons were used to extract pixel-based LST by employing MODIS and ASTER emissivity libraries and CORINE land cover classification. The LSTs were analysed against the in situ AT first with the correlation analysis. Except for December, the Pearson's correlation coefficients were statistically significant ( $0.449\text{--}0.654$ ,  $p \leq 0.001$ ). Seasonally adjusted linear regression models were applied to predict spatially continuous air temperatures ( $AT_p$ ) based on the extracted LST. Our results demonstrate that it is possible to predict urban ATs reliably - within ca. half-a-degree accuracy (MAE  $0.36\text{--}0.62$  °C). The prediction works best in spring, summer and autumn. It improves the capacity to produce reliable high spatial resolution AT information even if in situ observations are sparse.

## 1. Introduction

In the era of global change, accurate weather data of urban areas are needed to support management and planning purposes, and for the benefit of city dwellers. Temperature is often the most important weather parameter influencing our activities. It is considered in urban planning, selection of structural materials and architectural designs (Leyre et al., 2016; Lee and Oh, 2019). It has an impact on our health conditions (Shahmohamadi et al., 2011; USEPA, 2021). It also has a strong impact on the ecosystems (Grimm et al., 2008; USEPA, 2021). Considering the substantial influence of temperature on many aspects of our everyday life, accurate and easily available information of its spatio-temporal characteristics is important. The constraint of traditional thermometer-based temperature observations is that they provide information at fixed points only. Hence, a very dense network of thermometers would be needed to encompass the large spatial variation in temperature in and around urban environments. However, installing a dense network of weather stations in a region is not always economically and practically possible.

A common shortcut to overcome this information gap is to use remotely sensed land surface temperature (LST) data instead of air

\* Corresponding author.

E-mail address: [umer.alvi@utu.fi](mailto:umer.alvi@utu.fi) (U. Alvi).

temperature (AT) (Jin, 2012; Chen et al., 2006; Tsou et al., 2017). There are several satellite platforms that carry thermal infrared (TIR) sensors (Moderate Resolution Imaging Spectroradiometer (MODIS), Advanced Spaceborne Thermal Emission and Reflection Radiometer (ASTER) and Landsat, see USGS, 2021a; NASA, 2021a), and even ready LST data products (NASA, 2021b; ESA, 2021), but these are often of rather coarse resolution for detailed urban mapping. Of the openly available satellite products, ASTER and Landsat offer currently the best spatial resolution with 90 m and 100 m resolution, respectively. The ASTER products distributed from LP DAAC are produced from on-demand data acquisition requests and are not categorized by regular temporal ranges (USGS, 2021b) unlike Landsat, which offers regular acquisition. For the delivered product, Landsat TIR data are resampled into a 30 m grid.

The problem with the employment of LST in describing ambient thermal conditions in high spatial resolution is the large difference between the LST and the AT (Unger et al., 2009; Schwarz et al., 2012; Nichol and Pui, 2012; Azevedo et al., 2016). Hence, considering the LST as representing the temperature experienced by a city dweller may lead to inappropriate conclusions. We also demonstrate this temperature discrepancy in our study and provide a cost-efficient method to transform the remotely sensed LST into ambient AT using open data.

## 2. Urban temperatures and their derivation

One specific feature of urban climate is the temperature difference between the built-up areas and their neighbouring non built-up areas. This is called the Urban Heat Island (UHI). It has been a focus of research for many decades (Oke, 1987; Gallo and Owen, 1998; and Ng, 2015) and is a well-established phenomenon. Large scale urbanization produces urban heat (Pichierri et al., 2012) that could influence health and socio-environmental conditions (Alavipanah et al., 2015), and global warming (Chen et al., 2006). There are different main types of UHI: Surface UHI originates from different heat storing capacities of urban materials and refers to surface temperatures (Stathopoulou and Cartalis, 2007); Atmospheric UHI, caused mainly by the same factors than surface UHI, refers to air temperatures and is most intense at night (Oke, 1987; Voogt and Oke, 2003). Atmospheric UHI is further divided into two more categories: boundary layer UHI that is caused by anthropogenic forcing (Oke, 1995) with a scale of up to 100 km (mesoscale) (Stathopoulou and Cartalis, 2007; Barlow, 2014). Second is the canopy layer UHI, which is the air present between urban infrastructure (Oke, 1976). The canopy layer UHI extends up to roof top height and is affected by the nature of materials in the surroundings, shapes of urban structures and other anthropogenic causes (Oke, 1995). The surface and canopy layer UHIs are closely related, and this paper aims to produce new information on this relationship by developing a cost-efficient method to predict urban air temperature using open GIS data. The method could be cost-effectively applied also beyond the study area in predicting AT regardless of lacking or few in-situ observations.

Usually, UHI research is based on traditional weather stations (Tsou et al., 2017) but the scarcity of observation sites narrows down the measurement of UHI to low spatial resolution (Streutker, 2003). Few efforts have been made to solve these issues, and they come with pros and cons. Measurement of AT from batteries of smartphones using Android application (Overeem et al., 2013) is an example of collecting large temperature data. It proved to be difficult to confirm the reliability of those measurements, as many factors were involved including impacts of air temperature, location of the mobile phones (indoor and outdoor), impact of human body temperature, etc. (Overeem et al., 2013). Further examples have combined various statistical methods and traditional in situ temperature measurements in predicting spatially continuous air temperature ( $AT_p$ ) maps from observed air temperature ( $AT_o$ ) data (Hjort et al., 2011; Hjort et al., 2016).

One means to ease the collection of climatic data with high spatial resolution is to gather data under one platform in collaboration with different institutions or departments, as demonstrated in the Helsinki Testbed network in Finland. The effort focuses on the phenomena typical at meso-gamma-scale (1–10 km) that are difficult to observe with normal meteorological networks (Koskinen et al., 2011). Research infrastructure like this requires a large budget and is, therefore, not common. A combination of mobile measurements (Nichol and Wong, 2008; Schwarz et al., 2012) and fixed weather stations' measurements enables higher spatial resolution but lacks concurrency and is laborious for long-term data collection.

To address these issues, the use of remote sensing data for UHI studies has been suggested and applied. As remote sensing thermal sensors detect temperatures of surfaces rather than that of the air and therefore, they do not provide information directly comparable to ATs detected with thermometers (Unger et al., 2009; Caihua et al., 2011; Nichol and Pui, 2012). However, due to the lack of direct AT observations, it is common to refer to remotely sensed LST when estimating the thermal conditions of a region (e.g., Streutker, 2003; Jin, 2012; Feizizadeh and Blaschke, 2013; Mirzaei et al., 2020; Monteiro et al., 2021), potentially leading to misinterpretations.

We hypothesize that there is a semi-universal relationship between the surface temperature and the overlying air temperature over different land use/land cover (LULC) types on a 10–100 m scale. Such a relationship - when resolved - would allow determining air temperatures based on remotely sensed LSTs. A key aspect in the process of transforming the remotely sensed LSTs to ATs is to consider the emissivity properties of the particular surface type. This information is available in open spectral emissivity libraries if one knows the respective surface types. High-resolution openly available LULC datasets, such as CORINE (Coordination of information on the environment), can be used for resolving the surface types. Establishing such relationships between surface and air temperatures would allow estimating ATs through statistical modelling by employing remote sensing data alone, or with only few reference temperature observations. This would be beneficial in urban environments worldwide. We present here a model that can transform satellite-based surface temperatures to air temperatures, which are more relevant to human comfort.

## 3. Research aims

The rationale of this research is to develop and demonstrate a cost-effective, accessible, and easily deployable procedure whereby

continuous ambient AT could be estimated reliably using remotely sensed, openly accessible data without an extensive observation network. For this, we analyse and compare remotely sensed LSTs with data logger temperatures at 3-m elevation in an urban environment.

A combination of satellite based remotely sensed thermal infrared data, LULC data, and spectral libraries for emissivity information are employed for this purpose. All the data are open, consistent, and widely used, and therefore considered reliable.

In summary, the paper has the following research objectives:

- To produce a detailed urban surface temperature dataset at 20 m resolution by using Landsat 8 thermal infrared data, CORINE land cover data, and emissivity information from ASTER and MODIS spectral libraries.
- To compare and analyse the relationship between the calculated surface temperatures and observed air temperatures in different seasons and over varying land cover types.
- To produce a statistical relationship and model for estimating and predicting air temperatures based on Landsat-CORINE-emissivity-derived surface temperature, without a need for extensive in situ reference data.

#### 4. Study area

The study area is Turku, a coastal city in the southwest of Finland with around 190,000 inhabitants (Fig. 1, see also Fig. 2). Located in northern Europe between latitudes 60° and 70°N, Finland belongs to the Dfb and Dfc climate types in the Köppen-Geiger climate classification system (Peel et al., 2007). The southern coastal region along the Gulf of Finland of the Baltic Sea, where Turku is located, belongs to type Dfb (Peel et al., 2007). In southern Finland, summer arrives in late May, when the daily mean temperature exceeds +10 °C. In Turku, the highest temperature in 1981–2010 was measured on the 13th of July 2010, when temperature reached +32.1 °C at the Turku airport. The lowest temperature (−34.8 °C) was recorded on the 10th of January 1987 (Pirinen et al., 2012; FMI, 2020a). In southern Finland, heat waves occur typically for 10 to 15 days, during which the daily maximum temperature exceeds +25 °C. Autumn starts roughly at the end of September in the southwestern region when daily mean temperature falls permanently below +10 °C. Winter starts roughly in November in southwest Finland, when mean temperatures stay below 0 °C. Spring starts in April, when snow melts, daily mean temperature exceeds 5 °C, and the growing season commences (FMI, 2019).

Based on the data from the climate period 1981–2010, the mean annual precipitation in Turku is 720 mm. August is the wettest month with a rainfall of 80 mm, while April is the driest one with 30 mm of precipitation (Pirinen et al., 2012). Thirty percent of the annual precipitation falls as snow, and continuous snow cover lasts for three months, on average (Suomi and Käyhkö, 2012). The average wind speed is 3.4 m/s with dominating directions from the SW (17%) and S (14%) (Pirinen et al., 2012). During winter, the sea ice cover limits water vapor and heat transfer onto land, turning the climate in the region to a more continental mode (Suomi et al., 2012).

The land cover of the research area comprises manifold surface types, e.g., urban fabric including the port and light industrial area, the shore region of the Baltic sea with the complex archipelago with its numerous islands that exhibit many forest types from Boreal coniferous and mixed forest to rare oak forest of Ruissalo (Käyhkö and Skånes, 2008). Surrounding the city, there are agricultural lands and occasional lakes, the biggest of which is Littoistenjärvi (Fig. 1c). A rectangular study area of 216 km<sup>2</sup> was selected for the research, with Aura River flowing diagonally through the center of the research area to the Baltic Sea. The Turku Urban Climate Research Group (TURCLIM) of the Department of Geography and Geology of the University of Turku has set up a network of 75 temperature-humidity data loggers covering the region. The network, whose temperature observations are used in this study, is densest in the city center and gets gradually sparser further away (Fig. 1).

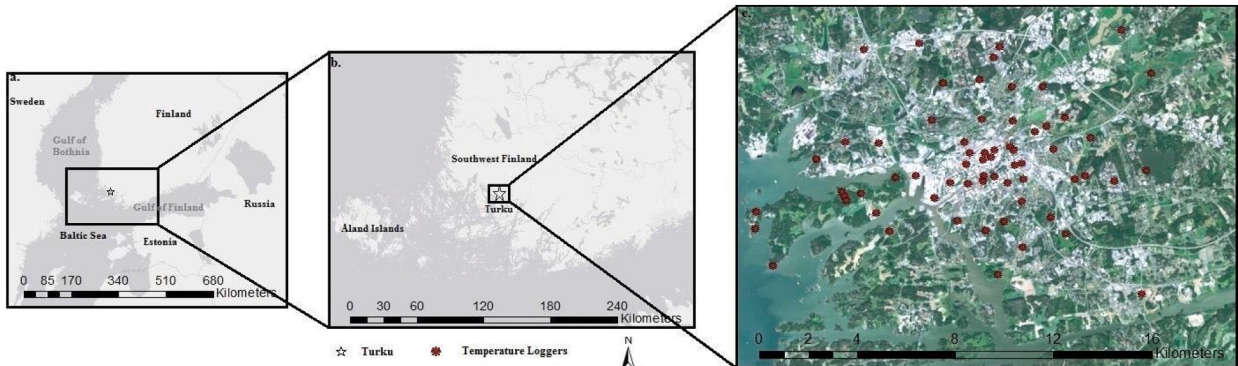
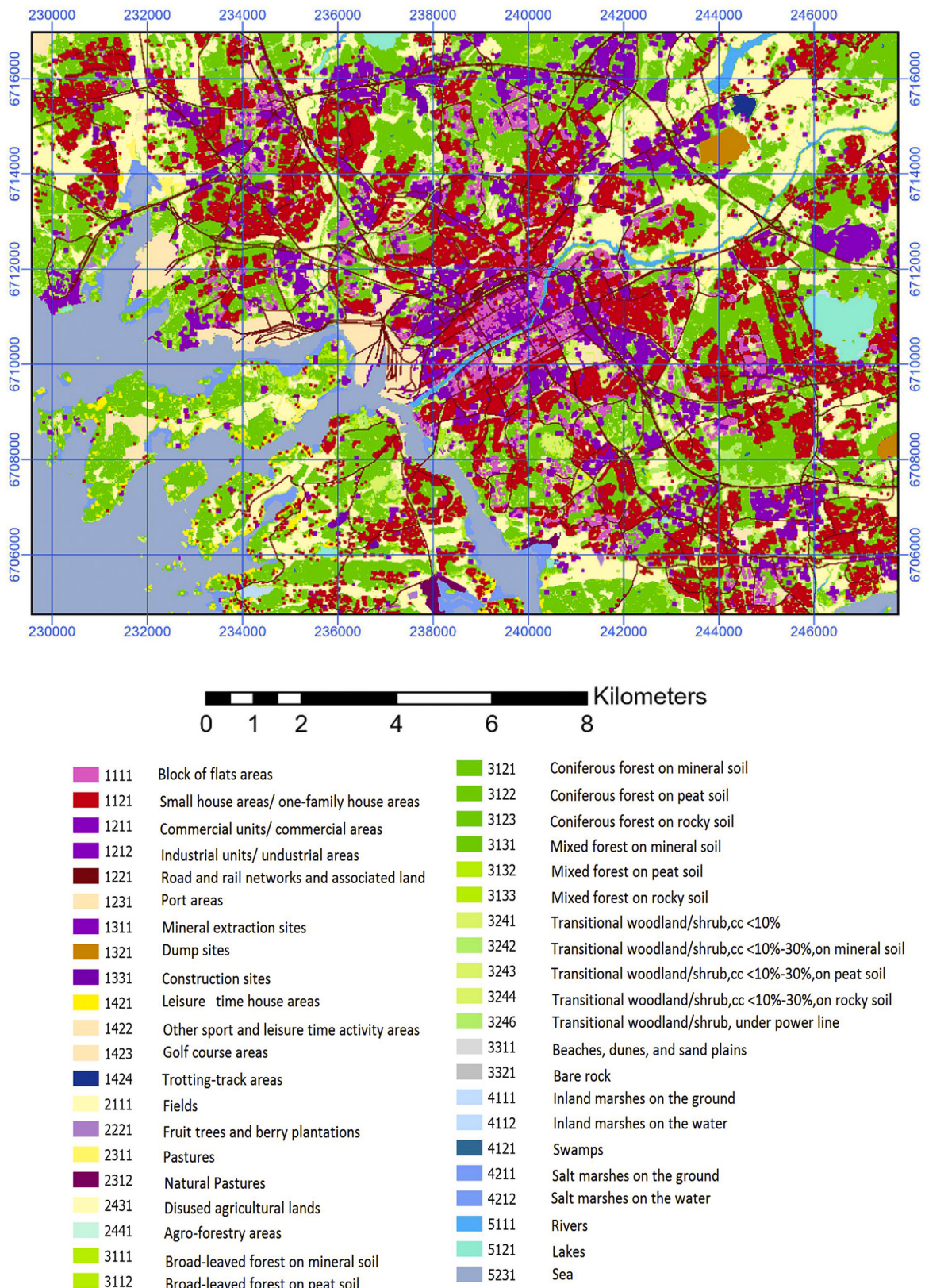


**Fig. 1.** The study area. (a) The location of the city of Turku on the coast of the Baltic Sea. (b) Turku city in the southwestern Finland with an extensive archipelago. (c) Research area on RGB (band combination 4 3 2) image of Landsat 8 on 3 July 2015 with red dots indicating the TURCLIM temperature logger sites. Built-up areas appear in pale colours. The city centre is in the middle. (For interpretation of the references to colour in this figure legend, the reader is referred to the web version of this article.)



(caption on next page)

**Fig. 2.** CORINE land cover classification (2012; Level 4) of the study area. Of the total of 48 CORINE classes, 42 are present in the study area and are listed in the legend.

## 5. Material and methods

The data consists of land cover data, satellite thermal infrared data representing different seasons of the year 2015, air temperature observations from the temperature-humidity sensors at 3-m elevation, and spectral libraries for emissivity corrections (Fig. 3).

### 5.1. Land cover data for emissivity mapping

Emissivity is the ratio of the energy radiated from a material's surface to that radiated from a blackbody. It is a dimensionless number between 0 and 1. The emissivity of a surface depends on the material and nature of the surface. The LULC emissivity information plays an important role in extracting LST, as even a minor error (0.01) in the emissivity value could cause a substantial inaccuracy in the extracted LST (see e.g., Sobrino et al., 2012). There are several methods available for emissivity correction for LST and e.g., the method based on the Normalized Difference Vegetation Index (NDVI) is in common use (Avdan and Jovanovska, 2016; Sobrino et al., 2004; Stathopoulou et al., 2007). For the current study, CORINE land cover (CORINE, 1994) Level 4 dataset (2012) with a grid size of 20 m was used Fig. 2). Based on independent field sample analyses (Härmä et al., 2015), the overall accuracy of CORINE LULC in Finland has been estimated at 61–93% depending on the number of classes and the reference data. The CORINE data originally have 48 classes, of which 42 were present in the study area. The most abundant classes in the study region were Small houses (class 2; 17%), Coniferous forests (class 24; 12%), Sea (class 48; 11%), and Fields (class 16; 10%) (Table 1). We assigned emissivity values to each class by interpreting the corresponding surface types from ASTER and MODIS spectral libraries (Meerdink et al., 2019; MODIS UCSB Emissivity Library, 1999). On Band 10 wavelength, different surface types may have the same emissivity value in the spectral library. Subsequently, the total number of different emissivity values for the 42 CORINE classes was 23.

### 5.2. Remote sensing data

In order to have as high spatial resolution as possible, we used data from Landsat 8 band 10, the thermal infrared sensor (TIRS 1), with a wavelength range of 10.60–11.19  $\mu\text{m}$ . We resampled the delivered 30 m grid (acquired at 100 m resolution) with nearest neighbour resampling to a 20 m grid to have a spatial match with the CORINE data. In order to minimise the risk of substantial changes in the urban structure during the studied time window, we selected the images from one calendar year. Due to the large seasonal differences in illumination and phenology in the study area, we considered it necessary to cover all seasons. However, as snow cover homogenizes the spatial differences in LSTs, we selected images from days without snow cover even during the cold season. Year 2015 meets this prerequisite well, as both March and December were snow-free. The preceding week prior to the acquisition was to be practically precipitation-free in all cases. This minimizes the possibility of moist land surface and ill-defined temperatures. The wind speed during the data acquisition time had to be low, as air flow causes blending of ATs through air mixing from the neighbouring areas (Suomi and Käyhkö, 2012). With these preconditions, five cloud-free images were available (Table 2). Later in the text, we refer to the images with the month of the image-specific satellite overpass time. By doing so, we are aware of the fact that the images represent the conditions of the moments they were taken, and only partly the conditions of the respective months as a whole. The data were at level L1T, orthorectified and radiometrically calibrated and best suitable for pixel level analysis. Landsat 8 OLI/TIRS has a 12-bit

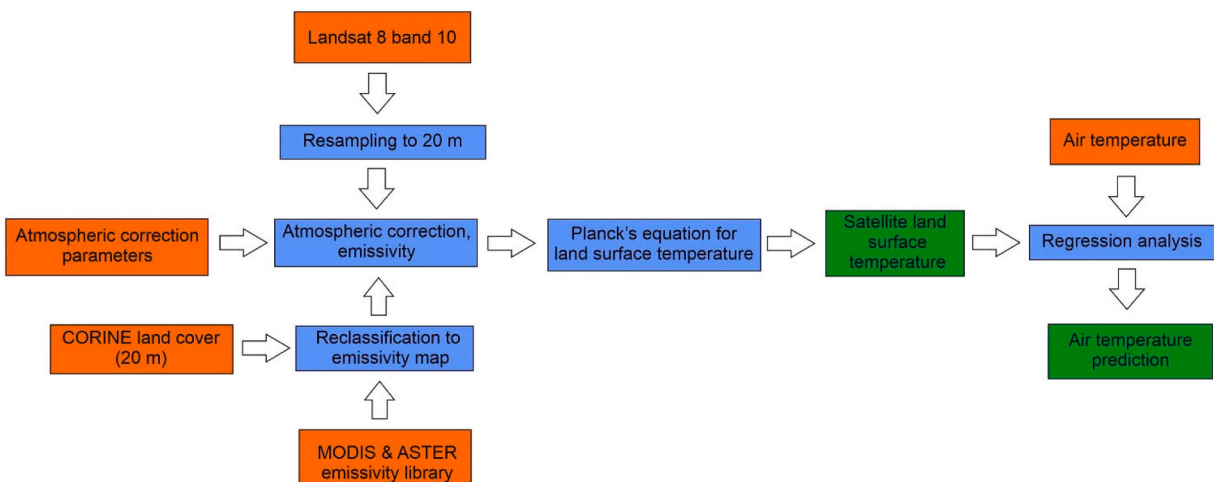


**Fig. 3.** Schematic diagram presenting the research flow, with data (in orange colour), processes/methods (blue) and outcomes/results (green). (For interpretation of the references to colour in this figure legend, the reader is referred to the web version of this article.)

**Table 1**

Emissivities determined for each CORINE class based on the ASTER and MODIS spectral libraries, plus the areal coverage (%) of the classes in the study area.

Class	Class name	Emissivity	Coverage %
1	Block of flat areas	0.953969	3.37
2	Small house areas / one-family house areas	0.959578	17.04
3	Commercial units / commercial areas	0.953969	5.02
4	Industrial units / industrial areas	0.953969	4.68
5	Road and rail networks and associated land	0.954243	5.29
6	Port areas	0.96507	1.56
7	Airports	0.969625	0
8	Mineral extraction sites	0.967516	0.37
9	Mines	0.967516	0
10	Dump sites	0.972071	0.34
11	Construction sites	0.954284	0.19
12	Leisure time house areas	0.960385	0.69
13	Other sport and leisure time activity areas	0.960385	0.81
14	Golf course areas	0.983186	0.31
15	Trotting-track areas	0.975351	0.08
16	Fields	0.975351*	10.21
17	Fruit trees and berry plantations	0.973057	0.06
18	Pastures	0.983186	0.26
19	Natural pastures	0.983186	0.19
20	Disused agricultural lands	0.975351	1.95
21	Agro-forestry areas	0.980839	0.01
22	Broad-leaved forest on mineral soil	0.973057	1.44
23	Broad-leaved forest on peat soil	0.973057	0.005
24	Coniferous forest on mineral soil	0.983433	11.61
25	Coniferous forest on peat soil	0.983433	0.12
26	Coniferous forest on rocky soil	0.983433	4.45
27	Mixed forest on mineral soil	0.980839	5.70
28	Mixed forest on peat soil	0.980839	0.05
29	Mixed forest on rocky soil	0.980839	0.41
30	Natural grassland	0.983186	0
31	Moors and heathland	0.982013	0
32	Transitional woodland/shrub, cc (crown cover) <10%	0.978122	5.33
33	Transitional woodland/shrub, cc (crown cover) 10–30%, on mineral soil	0.978122	3.40
34	Transitional woodland/shrub, cc (crown cover) 10–30%, on peat soil	0.978122	0.02
35	Transitional woodland/shrub, cc (crown cover) 10–30%, on rocky soil	0.978122	0.55
36	Transitional woodland/shrub, under power line	0.978122	0.39
37	Beaches, dunes, and sand plains	0.96105	0.005
38	Bare rock	0.956742	0.08
39	Sparingly vegetated areas	0.982013	0
40	Inland marshes on the ground	0.987921	0.06
41	Inland marshes on the water	0.987921	0.03
42	Swamps	0.981119	0.04
43	Peat bogs	0.981119	0
44	Salt marshes on the ground	0.988129	0.64
45	Salt marshes on the water	0.988129	0.74
46	Rivers	0.992657	0.57
47	Lakes	0.992657	0.82
48	Sea	0.993072	11.10

\* This emissivity value refers to July with an estimated 50/50 proportion of soil/grass. For August and October, an estimated 75/25 proportion of soil/grass gave an emissivity value of 0.970167, while 100% soil exposure for March and December gave a value of 0.967516.

radiometric range and consequently, 4096 levels of representation of the surface temperature conditions, and the delivered data products were scaled to 55,000 grey levels ([USGS, 2017a](#)). Therefore, it was well suited for calculating surface temperatures, as even minor differences in temperature could be detected as compared to the 8-bit data of TM and ETM+ ([USGS, 2017b](#)).

### 5.3. TURCLIM air temperature data

Air temperature measurements were recorded as a part of TURCLIM project; a total of 64 out of 75 logger sites were used for the year 2015 (see [Fig 1](#)). Temperatures were measured with Hobo Pro U23-001 temperature / relative humidity loggers at the interval of 30 min. The accuracy of the device is  $\pm 0.2$  °C at 0–50 °C. The T/RH loggers were installed 3 m above the ground with radiation shield protection. Three-meter elevation (instead of a standard 2 m elevation) is used in order to reduce the risk of vandalism as the loggers are located in public places. The overall type of the environment at each logger site has been classified as urban/semi-urban/rural. The number of available observation sites between the acquisition times varied slightly due to occasional gaps in the data ([Table 2](#)).

**Table 2**

Parameters describing the conditions during the satellite overpass. Landsat data acquisition dates (2015) and times, and the sun elevation were extracted from the Landsat metadata files. The meteorological parameters were acquired from the Finnish Meteorological Institution's Turku Artukainen weather station, including wind speed (average from sunrise to data acquisition time), precipitation (the latest 7 days), and temperature at the time of acquisition. Also included are the air temperature acquisition time and the number of observations from the TURCLIM network plus the sunrise time ([Auringon nousu- ja laskuajat Suomessa, 2019](#)).

	13 March	3 July	20 August	7 October	24 December
Satellite observation time (UTM + 2)	11:35	11:35	11:35	11:36	11:48
Sun elevation (degree)	26.0	51.7	41.4	24.0	5.9
Wind speed (m/s)	1.7	2.7	0.6	1.4	2.1
Precipitation (mm)	4.5	0.9	0.1	0	17.7
Temperature (°C)	4.9	27.2	21.4	6.1	4.4
Air temperature observation time (UTM + 2)	11:30	11:30	11:30	11:30	12
Air temperature observation points	63	61	61	62	64
Sunrise time (UTM + 2)	6:55	3:10	4:54	6:50	9:38

#### 5.4. CORINE LULC data and emissivity mapping

For emissivity data, CORINE class information and emissivity values for different materials from MODIS and ASTER libraries were analysed in detail. The emissivity values were assigned to the CORINE classes to convert them into emissivity maps representing different seasons. Some classes consisted of only one surface material, while others represented a combination of different surface materials. Consequently, some classes were assigned a single surface material emissivity value, while others were assigned a combination of values from different materials. Thereby, a lookup table (LUT; [Table 1](#)) was constructed for the CORINE based emissivity classification at the wavelength of 10.60–11.19 μm (for Landsat 8 band 10).

Continuous urban fabric, commercial and industrial buildings were assigned the average value of different kinds of building materials: brick, tile, lumber, masonry, pavement, stone, asphalt, and aluminum grate. Discontinuous urban fabric was assigned the average of building materials, grass, and trees. The inclusion of grass and trees in the discontinuous urban fabric was appropriate as the presence of a substantial proportion of vegetation is a typical property of Finnish landscape; in regional land use planning, environmental sustainability is considered important ([Environment, 2016](#)).

As there were no separate classes for different types of roads (such as small, unpaved, and main roads), urban transportation infrastructure that included roads, rail network and associated land was assigned with a single emissivity value as a combination of asphalt, soil, and dark metal. For the harbour area, an average emissivity value of concrete, black asphalt, bricks and masonry was used, while the airport class assigned an average of concrete and black asphalt. Crop fields were assigned different emissivity values in different seasons based on the varying proportions of soil and vegetation due to growth, harvesting and tillage (see [Table 1](#)). All other classes including vegetation were considered having equal emissivity independent of the season, as the forests in the study area consist mostly of coniferous trees.

#### 5.5. Extracting land surface temperatures (LST)

For extracting LST, the radiative transfer equation was used ([Sobrino et al., 2004](#)). The data were in the form of raw DN values and rescaled to top of atmosphere (TOA) radiance L by using the rescaling factors provided with the delivered data product, using the ([Alavipanah et al., 2015](#)) ([USGS, 2019](#)).

$$L_\lambda = ML(Q_{cal}) + AL \quad (1)$$

Where:  $L_\lambda$  = Top of atmosphere radiance,  $ML$  = Band specific multiplicative rescaling factor,  $Q_{cal}$  = pixel value (Digital Number) and  $AL$  = Band specific additive rescaling factor.

Atmospheric correction was performed using the following expression ([Sheng et al., 2017](#)):

$$B(Ts) = \frac{L_{sensor} - L \uparrow}{\varepsilon \tau} - \frac{1 - \varepsilon}{\varepsilon} L \downarrow \quad (2)$$

Where:  $B(Ts)$  = Radiance of the blackbody target,  $L_{sensor}$  = At sensor radiance,  $\varepsilon$  = Emissivity,  $\tau$  = Atmospheric transmittance,  $L \uparrow$  = Upwelling radiance and  $L \downarrow$  = Downwelling radiance.

Above mentioned atmospheric parameters were calculated with the online atmospheric correction parameter calculator ([ACPC, 2019](#); [Barsi et al., 2003](#); [Barsi et al., 2005](#)), Finally LST was calculated using the Planck's equation ([Sheng et al., 2017](#); [Barsi et al., 2005](#)).

$$LST = \frac{K2}{\ln \left( \frac{K1}{B(Ts)} + 1 \right)} \quad (3)$$

Where:  $LST$  = Land surface temperature,  $K1$  and  $K2$  = Band specific calibration constants,  $B(Ts)$  = Atmospheric and emissivity corrected radiation.

## 5.6. Statistical methods

For analysing the characteristics of the correlation between surface and air temperature, both Spearman's rank correlation and Pearson's correlation were used. Pearson's correlation coefficient tells about the linear relationship between the variables, while Spearman's correlation explains both linear and nonlinear correlations (Schwarz et al., 2012). For the regression analysis, we tested two potential and relevant explanatory variables that are easy to produce from open data regardless of the location, namely the LST, and the Area Solar Radiation derived with the aid of Digital Elevation Model (DEM). The Area Solar Radiation did not show statistically significant correlation with the surface temperature nor with the air temperature, probably due to the gentle topography and the disturbing effect of the urban structure, and hence, only the LST was included as the explanatory variable in the regression analysis (see Supplementary data). For the surface temperature, the pixel values at the TURCLIM logger sites were used without utilizing any buffer as Landsat 8 TIRS 1 (band 10) is acquired at 100 m (30 m in the delivered data product) resolution, functioning itself as a 100 m buffer. These LST values and the respective logger ATs for all the five satellite acquisition days were separately analysed for correlations. Based on the high Pearson's correlation coefficients (see Table 3), we used a linear regression model for predicting AT with the LST. The ENTER option was selected, i.e. the explanatory variable was automatically included in the model regardless of its statistical significance. To easily understand the thermal behaviour of the land cover types on the logger sites, the point locations were classified into three categories in the scatter plot: urban, rural and semi-urban. This classification was based on the field visits and visual interpretation of the high resolution images of Turku city.

## 6. Results

### 6.1. Emissivity mapping and land surface temperatures

Land surface temperature (LST) maps highlight the substantial spatial temperature variations of different land surfaces, especially in summer months (Fig. 4). In July, the range between the lowest and highest surface temperature was 31 °C. The highest surface temperature of 47.3 °C was observed on dark coloured roof of a large building near the sea. Hence, sea proximity did not seem to lower the surface temperature. Highest surface temperatures were generally observed on large asphalt areas and dark flat roofs. The lowest surface temperature in July was observed on the sea.

Compared with July, August had a similar kind of temperature pattern on land surfaces but with a smaller temperature range and lower maximum and minimum temperature. Towards the end of summer, the temperature difference between the sea and land started to diminish as land temperatures were gradually dropping. However, the sea still kept mostly cooler than the land surface. An interesting high temperature anomaly was spotted in a small open field area on the island of Ruissalo (see the arrow in Fig. 4). We interpreted this as a local anthropogenic influence due to abrasion of vegetation on the site of the Ruisrock festival (held on 3–5 July), and the subsequent high LST of bare soil.

In March and October, the highest observed temperatures were 15.3 °C and 16.6 °C, respectively. In both of these months, temperature hotspots remained the same as in summer months, but with smaller temperature range. In October, the sea surface was warmer than the majority of the land areas. The shallow water close to the shore was cooler than deeper water with higher heat capacity. Similarly, in March, some sheltered bays exhibited the lowest sea surface temperatures (SST), as they may have been partially ice-covered at times.

The lowest LSTs were observed in December. In early winter, SST was much higher than the LST and high temperatures were observed along the edges of the Islands and Turku city shorelines. During all the studied months, lake and river water temperatures deviated somewhat from the seasonal temperature trend of the sea water due to small specific heat capacity; in August and July, surface water in lakes and rivers was warmer than the SST, while in March, October and December, this pattern reversed.

To corroborate the validity of the results, the extracted SST was compared with a reference SST from a research buoy located near the Archipelago Research Institute on Seili island (60°15.35 N 21°57.11E, WGS84). The data are available for ice-free months and hence, can be used as a reference for the July, August and October cases. The extracted temperatures correspond very well with the reference temperatures (Table 4). The 1.5 h time difference between the Landsat overpass and the buoy temperature reading is not a substantial source of error, as buoy data from the wave observation site Baltic Sea Proper (59°15' N 21°00' E) (FMI, 2020b) with hourly sampling frequency indicate that the sea surface temperature on the respective days changed only by 0.1 °C between 11:30 and 13:00 h.

**Table 3**

The results of the correlation and linear regression analyses.

	13 March	3 July	20 August	7 October	24 December
n	63	61	61	62	64
Spearman's rho correlation coefficient	0.612***	0.469***	0.447***	0.428***	0.261*
Pearson's correlation	0.654***	0.578***	0.529***	0.449***	0.207
Linear regression r <sup>2</sup>	0.4281	0.3338	0.2798	0.2017	0.0426

\* Correlation is significant at the 0.05 level (2-tailed); \*\* Correlation is significant at the 0.01 level (2-tailed); \*\*\* Correlation is significant at the 0.001 level (2-tailed).

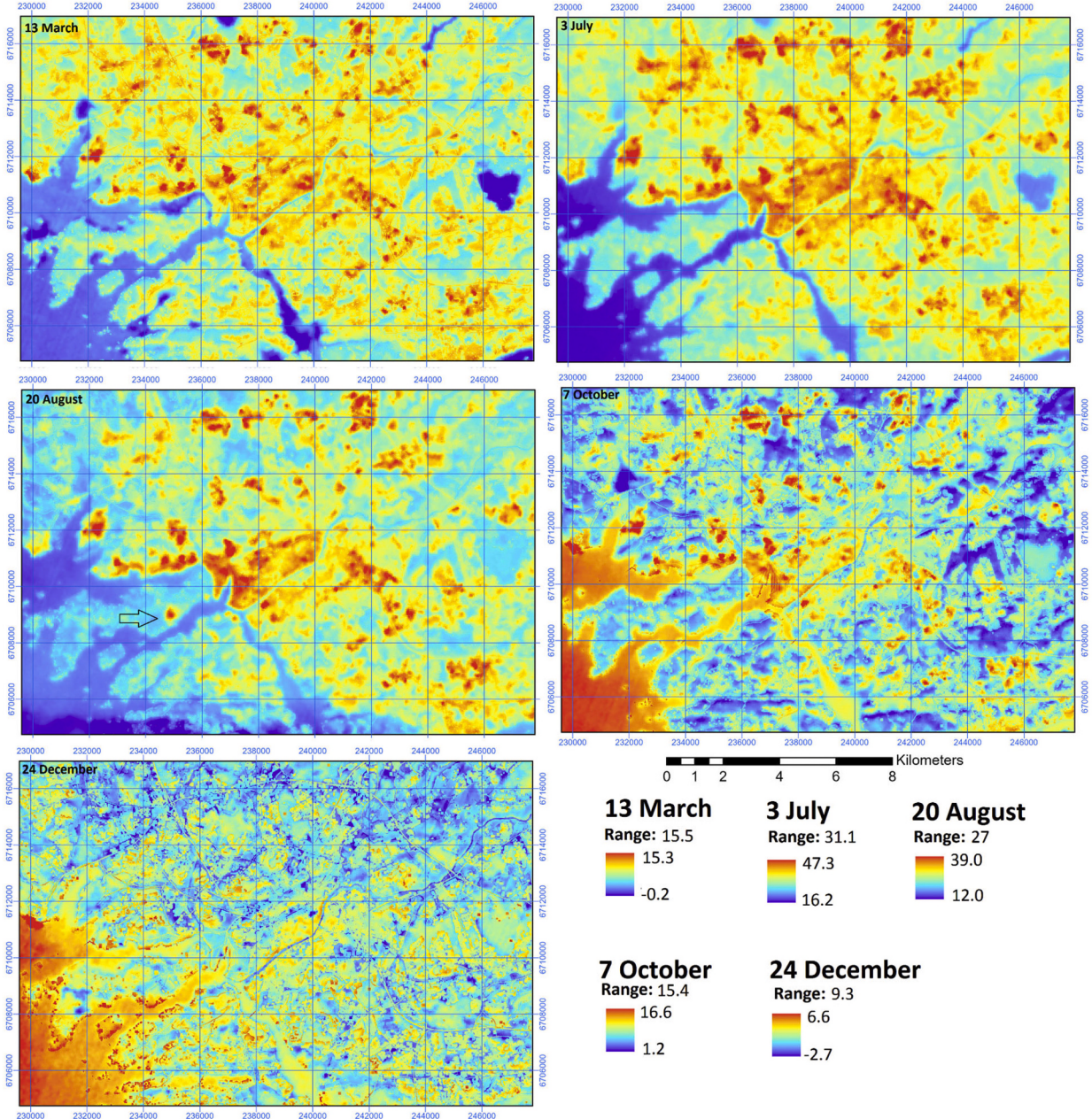


**Fig. 4.** Land surface temperatures (LST) at 20 m spatial resolution produced with Landsat 8 band 10 and emissivity information derived from MODIS and ASTER emissivity libraries adjusted to CORINE land cover classes. The arrow on the August map refers to a hotspot high LST anomaly not visible in other months (see text). Notice that the different moments in time cannot be compared directly with each other due to the different temperature scales (for highlighting the spatial pattern). For comparison between the seasons, see Fig. 8.

**Table 4**

Comparison of the in-situ temperature observations with Sea Surface Temperature (SST) values extracted from Landsat data.

	3 July	20 August	10 October
Buoy temperature °C (2 m depth) at 1300 h (UTM + 2)	16.94	19.3	13.22
Extracted SST °C at 11:30 (UTM + 2)	15.74	19.33	13.03
Temperature difference °C (observed – extracted)	+1.2	-0.03	+0.19

For corroborating the validity of the extracted LST in land areas, FMI road temperature data points Turku and Kaarina were employed. The data are from the FMI open data service. The surface temperature data acquired with a sensor sitting inside the asphalt represents solely the road surface temperature while the Landsat 100 m pixel value is a combination of road surface temperature and the temperature of other land cover types on the road sides. Therefore, the differences between the two temperature values can be large especially in the warm season with high solar irradiance and should be used with careful sites-specific consideration as a reference for satellite LST ([Table 5](#)).

## 6.2. Relationship between land surface temperatures and air temperatures

The strongest Spearman's correlations between the surface and air temperature were observed in March followed by July, August, October ( $p \leq 0.001$ ) and December ( $p \leq 0.05$ ). Pearson's correlation test results showed the same pattern, but the correlation for December was not statistically significant. In summary, the correlation results indicated a linearly increasing function with statistically very significant correlation ( $p \leq 0.001$ ) in all months apart from December, when only a monotonic statistical relationship was observed ([Table 3](#), [Fig. 5](#)).

In the scatter plot (see [Fig. 5](#)), the urban, semi-urban and rural classes form quite separate clusters along the regression line especially in the summer months. Urban classes show high surface and air temperature, while rural classes typically have lower temperatures. The semi-urban class sits between the urban and rural classes. The cold AT outliers specifically in the cold season are interpreted to result from local cold air pooling into topographic lows.

Using the linear regression equations ([Fig. 5](#)) for different months, spatially continuous  $AT_p$  maps were produced ([Fig. 6](#)). The spatial distribution of temperature variation in the  $AT_p$  was similar to the LSTs ([Fig. 4](#)), but the overall temperature range was radically smaller, being between 1.3 °C (Dec) and 3.3 °C (other months) in the area, as compared to ca. 9 °C (Dec), 15 °C (Mar, Oct) or 30 °C (Jul, Aug) observed in LSTs. In other words, the air temperature range was only ca. 1/5 to 1/10 of the surface temperature range, demonstrating the reliability challenges in using direct LSTs as an estimate of ambient regional temperatures.

For testing the accuracy of the predicted air temperatures ( $AT_p$ ) calculated using the regression equation, we calibrated a linear regression model for each month with 51–54 observation sites, excluding ten observation points that were used for assessing the regression validity. The equations acquired in model calibrations were used to predict the values for the ten reference points. The Mean Absolute Error (MAE) of the ten predicted values was around half-a-degree (0.36–0.62 °C, see [Fig. 6](#)). The corresponding Root Mean Square Error (RMSE) values of the regression equations for the validation data were 0.39–0.57 °C.

In addition to land areas, we tested the performance of our linear regression model also on the sea area and the archipelago by comparing the  $AT_p$  with the  $AT_o$  at the Seili buoy. The buoy ATs differ somewhat from the  $AT_p$ , especially in July ([Table 6](#)). The probable reason for this is that the AT observation sites used in model calibration were located in the land areas and consequently, the model performance is better there.

## 7. Discussion

The current study aimed at assessing the capability of open data in predicting urban AT with high spatial resolution. The adjacent land surface temperatures (LSTs, based on Landsat and CORINE data) and  $AT_o$  differ from each other by site characteristics and season ([Fig. 5](#)), calling for a model that takes into account this complex relationship. We were able to build a linear regression model for predicting air temperatures at any point in the area by employing Landsat thermal data, land use / land cover data and spectral emissivity libraries in conjunction with high-resolution temperature observations. This regression model is capable of predicting AT quite accurately, providing ca. half-a-degree accuracy. An important factor that allowed us to achieve good prediction accuracy was the dense network of TURCLIM observation sites. [Hjort et al., 2011](#) suggest that for reliable modelling, all environmental conditions present in the region should be included in the coverage of the data network. In our study, the dense constellation of the logger network successfully covered the existing surface types, and different urban thermal environments and thus, allowed an analysis of the complex thermal nature of the area. In conjunction with this study, we developed a lookup table ([Table 1](#)) that gives the emissivity values for the

**Table 5**

Comparison of the Land Surface Temperatures (LSTs) extracted from Landsat data with the observed road surface temperatures by the Finnish Meteorological Institute (FMI).

		Extracted LST °C	FMI Land Surface Temperature °C	Temperature difference °C (Extracted – Observed)
7 October	Turku	10.0	12.1	-2.1
	Kaarina	8.2	11.9	-3.7
20 August	Turku	29.5	35.5	-6.0
	Kaarina	25.2	35.7	-10.3
24 December	Turku	1.0	2.6	-1.6
	Kaarina	1.3	1.5	-0.2
13 March	Turku	8.3	9.3	-1.0
	Kaarina	7.4	8.9	-1.5
3 July	Turku	37.6	44.0	-6.4
	Kaarina	32.2	44.1	-11.9

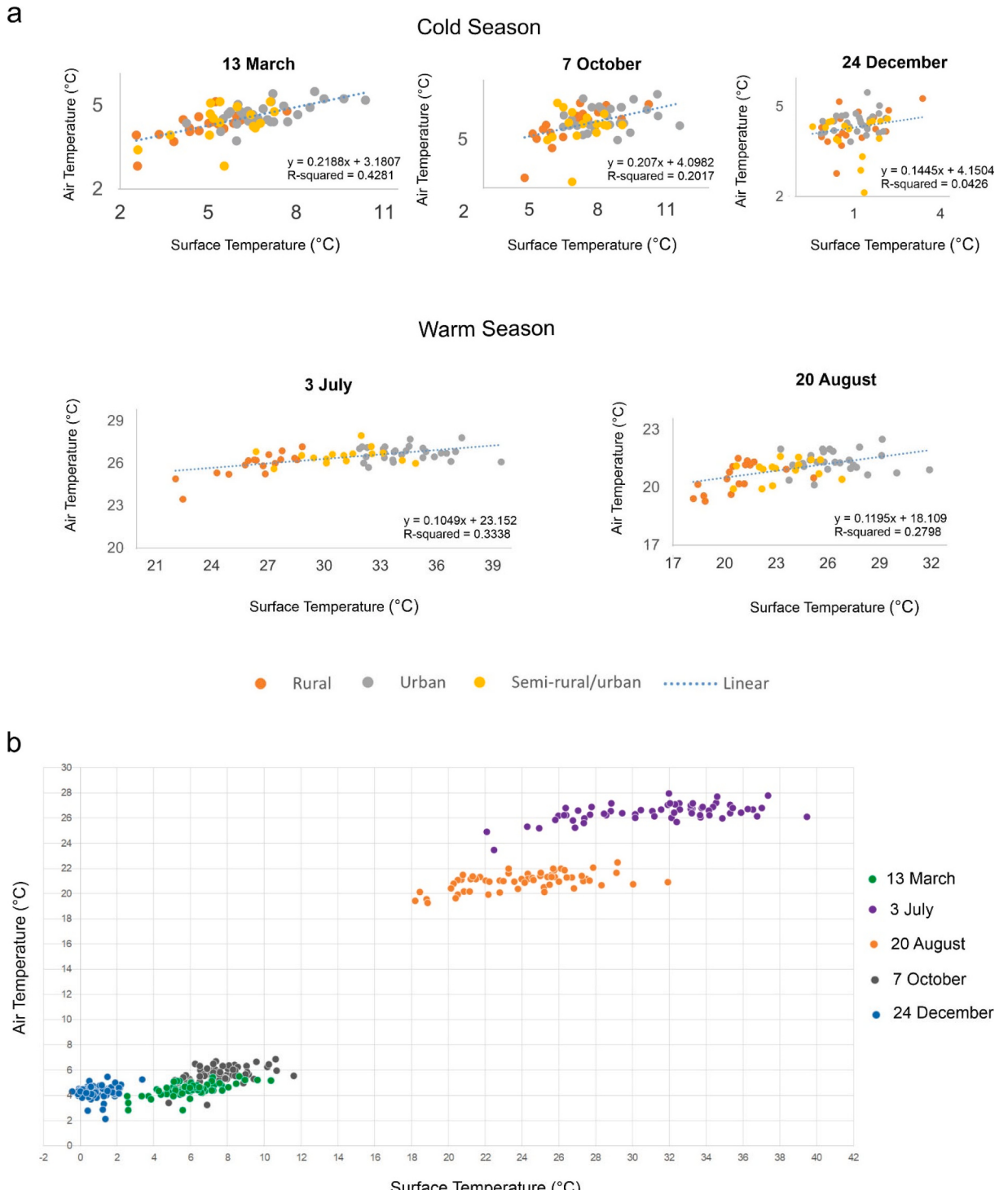


**Fig. 5.** a. Scatter plots showing the relationships between the Landsat-derived surface temperatures (LST) and observed air temperatures ( $\text{AT}_o$ ) of the three different types of environments at TURCLIM observation sites at five momentary situations in 2015. The different land cover types are located discordantly within the scatter cloud during summer, reflecting the impact of differential surface heating. During seasons of low sun angle (specifically in December), the differences between land cover types are subdued. b. Same as 5a, but with a common scale for x and y axes, and without land cover type information. During summer, the large deviation in LST values (due to high solar irradiance) as compared to air temperature variation is clearly visible in the elongated form of the respective scatter clouds.

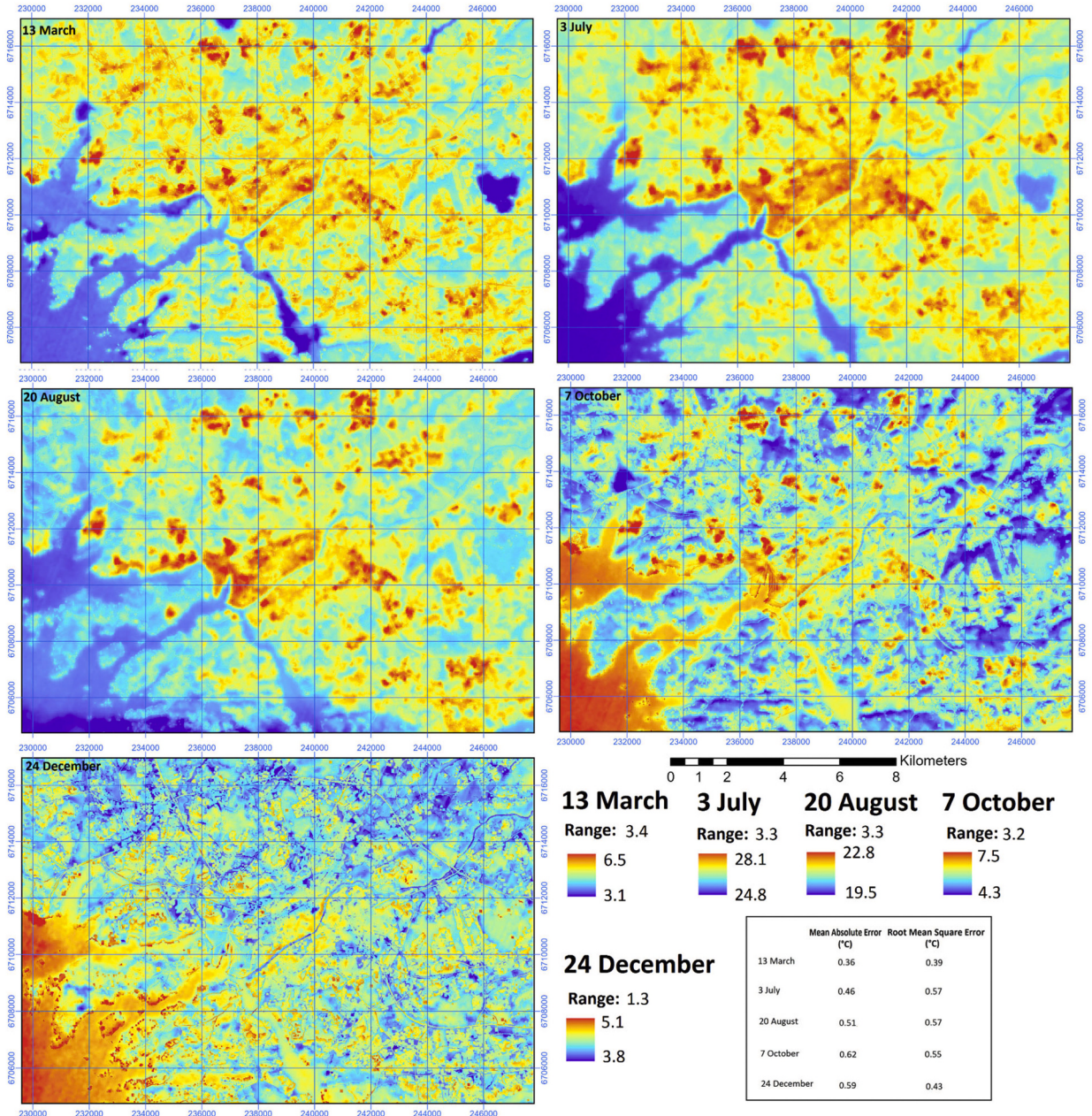


**Fig. 6.** Air temperature predictions ( $^{\circ}\text{C}$ ) at 3 m height with 20 m spatial resolution, based on Landsat 8 band 10 and CORINE land cover data. Notice that the different moments in time cannot be compared directly with each other due to the different temperature scales (for highlighting the spatial pattern). For comparison between the seasons, see Fig. 8. The mean absolute error for the ten predicted validation points, and the root mean square error values for the calibration data are also presented.

**Table 6**

Comparison of the predicted air temperature ( $\text{AT}_p$ ) with the observed air temperature ( $\text{AT}_o$ ) over the sea.

	3 July	20 August	10 October
Buoy air temperature ( $^{\circ}\text{C}$ ) at 12:30 (UTM +2)	20.8	18.7	6.2
Predicted air temperature ( $^{\circ}\text{C}$ ) at 11:30 (UTM +2)	24.8	20.3	6.6
Temperature difference ( $^{\circ}\text{C}$ ) (predicted – observed)	-4.0	-1.6	-0.4

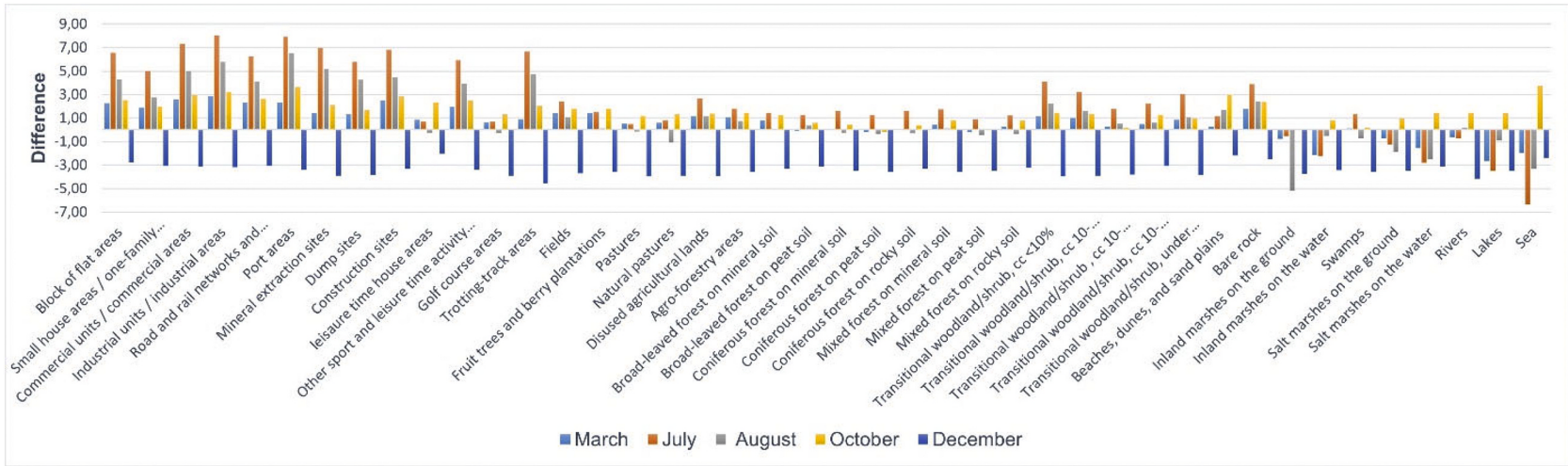


**Fig. 7.** Temperature differences between LST and AT by CORINE class and season (month). The bars illustrate the average value of LST minus  $AT_p$  for all pixels in each CORINE class for the five studied moments in time. Notice the large positive difference values (LST much higher than air temperature) among the urban classes on the left end of the graph, and the anomalous (negative) behaviour of the December values with air temperatures higher than LST in all CORINE classes. See text for further discussion.

wavelength range of 10.60–11.19  $\mu\text{m}$  (Landsat 8 band 10). In the table, emissivity values for each CORINE land cover class are assigned from the information of ASTER and MODIS spectral libraries.

### 7.1. Air temperature modelling

The season-specific and CORINE class-specific anomalies in the temperature differences between the LST and the AT (both observed and modelled) (see Figs. 5 and 7) clearly demonstrate that satellite-based LST cannot be directly used as a measure of ambient air temperature in urban areas. This challenge can be overcome by relating the LST to AT using statistical methods, as demonstrated earlier by e.g., Nicole and Pui Hang 2012 using ASTER data, and Schwarz et al., 2012 using airborne thermal data. These examples, however, include some shortcomings such as the case-specific limited availability of ASTER and airborne data. The Landsat data used in this study provide regular global coverage combined with rather fine spatial resolution.

The results of our linear regression model also demonstrate the applicability of the statistical methods by being able to convert the

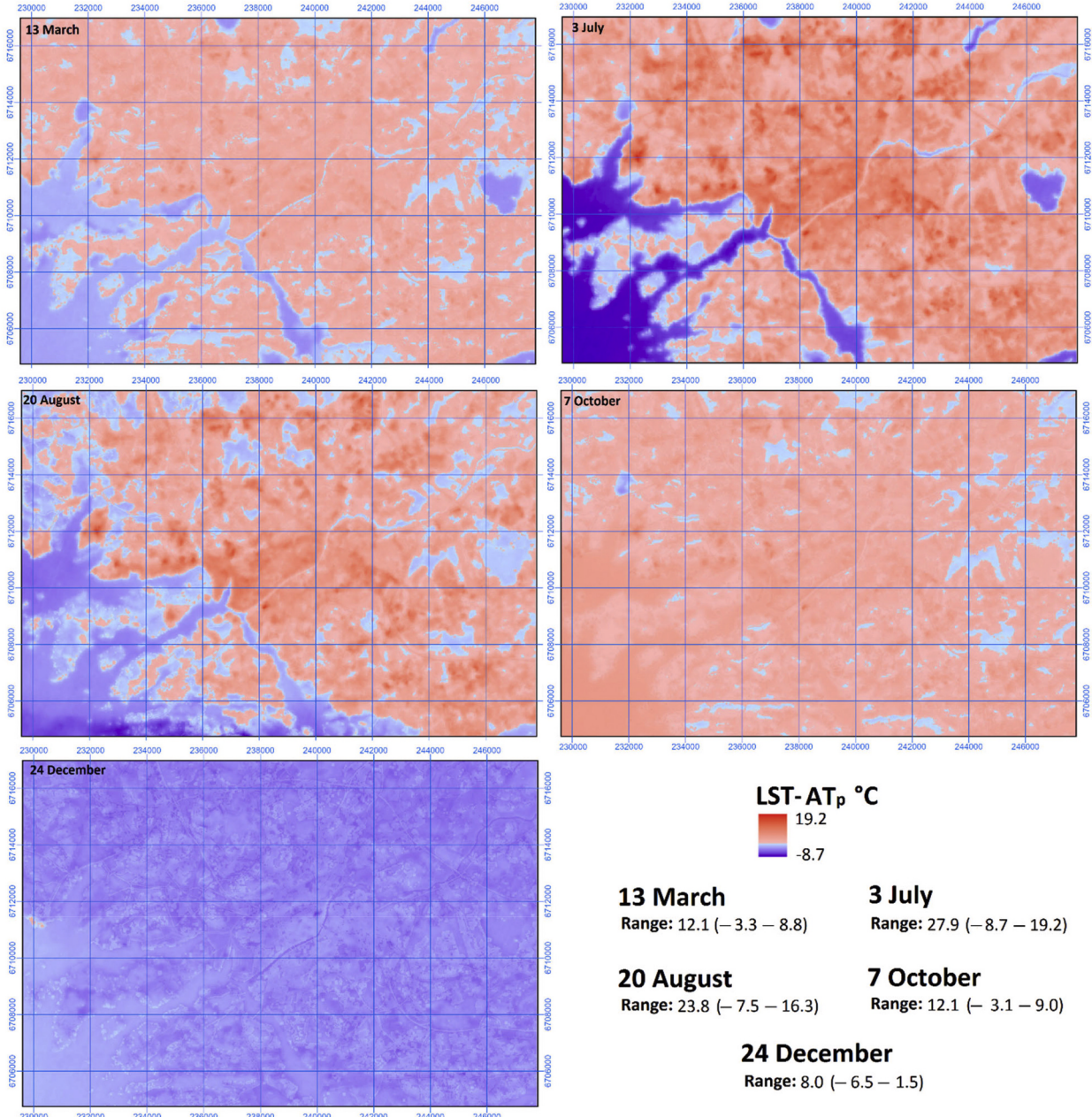
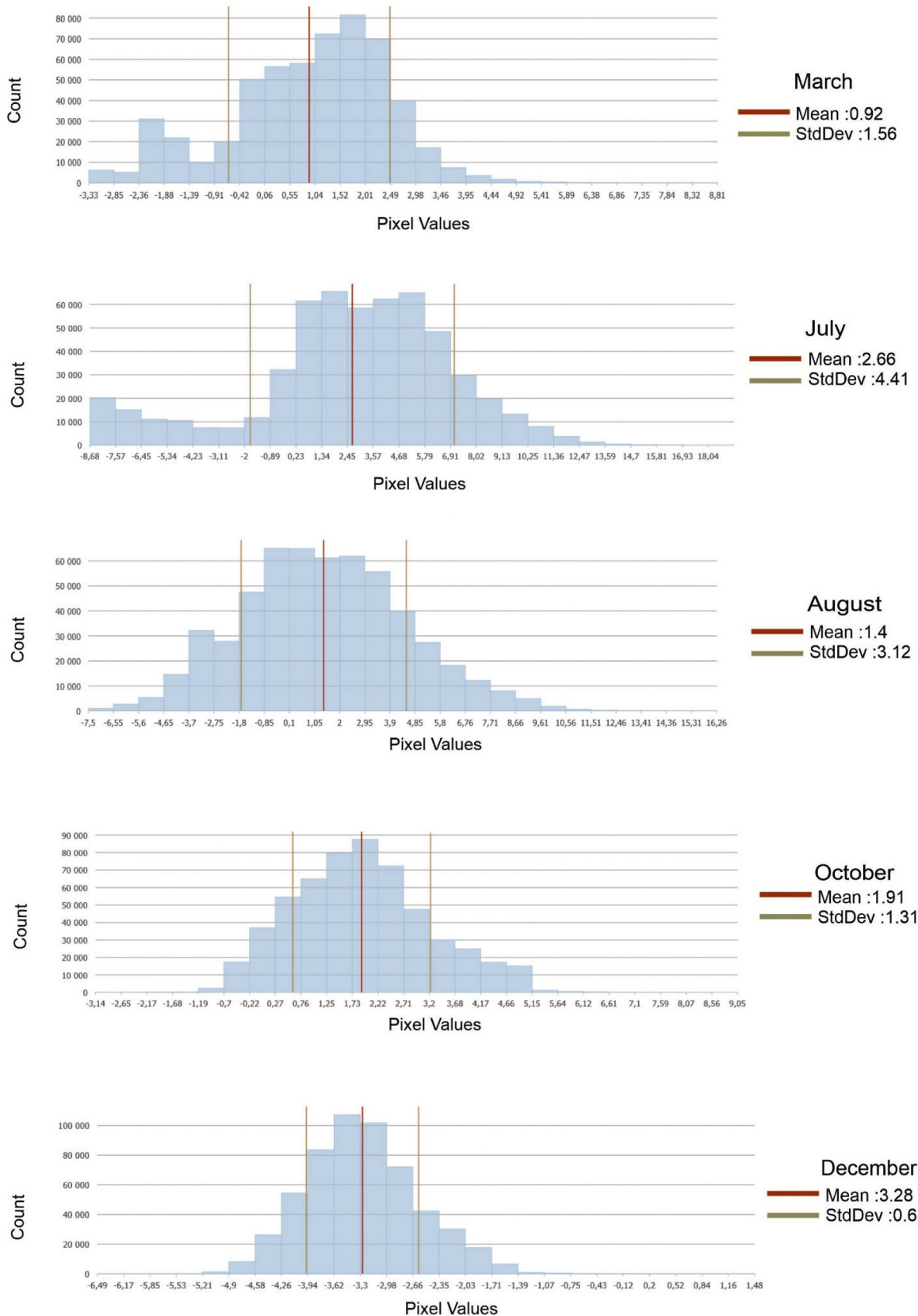


**Fig. 8.** Ranges between land/water surface temperature (LST/SST) and predicted air temperature (AT<sub>p</sub>) in different moments in time (~seasons).



(caption on next page)

**Fig. 9.** Distribution of pixels for different magnitudes of surface and air temperature difference (LST minus AT<sub>p</sub>) range.

LST to ambient air temperature with ca. half-a-degree accuracy (see Fig 6). Compared to other studies (e.g., Flores and Lillo, 2010; Dos Santos, 2020; Yang et al., 2017), our methodology is more accurate as reflected by the clearly lower RMSE values. However, our results also demonstrate the impact of seasonality in model performance due to thermophysically different conditions between the seasons. The impact of seasonality on the model efficiency has also been found e.g., by Rodríguez-Lado et al., 2007. Their study, carried out in São Paulo, shows clearly lower fits in (austral) winter months, a phenomenon that was observed also in our study. In our study area, the potential temporal temperature differences are as their largest in winter. On a cloudless morning (a prerequisite for good quality Landsat data) in December, AT in Turku can vary between  $-25^{\circ}\text{C}$  and  $+7^{\circ}\text{C}$  depending on the synoptic weather situation (Heino and Hellsten, 1991). This large variability sets a challenge especially for developing a model that would fit for all potential winter conditions.

The basis for the AT<sub>p</sub> consisted of the LST datasets that were generated using the radiative transfer equation and Planck's equation (see Methodology section). As stated earlier, the correctness of the emissivity parameter is crucial for getting reliable LSTs (Sobrino et al., 2012). We are aware that there is a risk of inaccuracies when using the emissivity values from spectral libraries and assigning them to the CORINE classes. There are also other unknown factors in addition to LST affecting the AT that have not been retrieved with the current modelling. These deserve further analyses in future research. Despite the uncertainties, the AT<sub>p</sub> based on Landsat, CORINE and spectral libraries was found to be a cost-efficient and reliable method that can be employed widely, especially during warm seasons.

## 7.2. General patterns of seasonal temperature differences

In general, rather large differences between the LST and the AT<sub>o</sub> as well as between the LST and the AT<sub>p</sub> were detected in all months (see Figs. 5, 7 and 8). Spatially, the differences between LST and AT<sub>p</sub> also varied substantially depending on both the CORINE class (see Fig. 7) and the season (Fig. 8). The largest differences were found on urban surface types, where surface temperatures were typically clearly higher than the adjacent ATs, especially in summer months (see Fig. 7). On water bodies, the differences were almost as large, but the direction varied seasonally: in summer, the ATs were higher than the sea surface temperatures (SST). The range of temperature difference was largest in summer months and smallest in winter (Fig. 8). Contrary to the other months, air temperature in December was higher than the surface temperature on all CORINE classes (see Figs. 7 and 8). This is somewhat coincidental, as the image acquisition day was rather warm ( $4.4^{\circ}\text{C}$ ) compared to the long term average of daily maximum temperature for December ( $-0.1^{\circ}\text{C}$ , Pirinen et al., 2012).

The histograms demonstrating the pixel by pixel distribution of differences between the LST and AT<sub>p</sub> show relatively normal distribution in October and December (Fig. 9). In March, the distribution is negatively skewed, whereas in July and August, the distributions are rather flat especially in the middle part of the value continuum. The secondary peaks in the lowest part of the value continuums of March, July and August represent the relatively cool surfaces of the water bodies. Fig. 9 also reveals that, similarly to the range (Fig. 8), summer months also had larger standard deviation than winter months in the differences between LST and AT<sub>p</sub>, reflecting the impact of high irradiance in summer.

## 7.3. Season-specific temperature differences

In late winter / early spring (March), urban areas were generally warmer than rural areas for both LST and AT. The magnitude of this spatial difference is larger in LST than in AT<sub>p</sub> (see Figs. 4 and 6). We interpreted the relative warmth of the urban areas as a result of the heat storage capacity and anthropogenic heat of urban infrastructure.

In summer, the intensive solar irradiance has a strong influence on LSTs. Consequently, the different land cover types - urban, semi-urban and rural - show clear differences in LSTs, while the ambient air temperatures do not vary as much. This is clearly demonstrated in the scatter plots of the July and August data (Fig. 5). Vegetation cover and LST are known to be negatively correlated (e.g., Procházka et al., 2011) and the relatively low temperatures in the rural and semi-urban areas in our study were also interpreted as a result of vegetation cover (see Zaki et al., 2020) (see Figs. 4 and 6). A similar cooling effect of vegetation has been identified also in the study by Alavipanah et al., 2015 and Harun et al., 2020. The differences between LSTs of the surface types are enhanced by urban impervious surfaces that have good thermal conductivity and high solar heat storage capacity.

In the autumn (October), there is a clear flip in the temperatures between sea and land areas in that the sea remains relatively warm due to the large heat storage capacity, while the land areas are getting cooler. The temperature difference range between LST and AT gets narrower compared to summer. In the scatter plot (Fig. 5), the temperature points of different surface types are getting more closely packed than in summer. We interpret this as a result of decreasing direct solar heating in the autumn and subsequently, smaller temperature differences between various surface types. UHI hotspots are yet clearly detectable.

In early winter (December) the sea areas are still warmer than the land areas, but the difference is not as large as in October. UHI areas are hardly detectable. All in all, the temperature range across the area is smaller than in any other season for both LST and AT. The different surface type points in the scatter plot (Fig. 5) are mixed, indicating little difference between the classes due to low solar irradiance. This also means that the CORINE classes across the study area may not have as consistent temperature behaviour as in other seasons. Of all the studied moments of time (seasons), December stood out as an anomaly in that regardless of the CORINE class, the average values of the pixel-by-pixel temperature differences between LST and AT (LST - AT<sub>p</sub>) were always negative (see Fig. 7 and 8).

We interpret this as a result of a mild surface inversion situation due to low solar irradiance.

#### 7.4. Open emissivity and temperature data

Coarse spatial resolution remote sensing data such as MODIS (1 km) have been widely used for estimating LST (e.g., Flores and Lillo, 2010 and Georgiou and Akçit, 2017). Kilometer-level resolution, however, is not adequate to unravel spatial temperature variation in complex urban infrastructure. The use of high-resolution Landsat data with CORINE based emissivity of 20 m grid has lower pixel level land cover heterogeneity as compared to coarser spatial resolution MODIS data, which have been demonstrated to cause an overestimate of LST seasonal fluctuations over heterogeneous land cover (Georgiou and Akçit, 2017).

With its 48 land cover types, CORINE offers detailed land cover information. It has numerous classes for different vegetation types and consequently, different emissivity values especially for forests, riversides and the coast. This property makes CORINE applicable for accurate temperature extraction also of non-urban green areas.

CORINE classification is available for the whole of Europe (see Copernicus, 2021). However, different regions in Europe have different constellations of landscapes, environments and land cover material types. Therefore, when applying our method in other parts of Europe, this fact ought to be kept in mind, although the employed average values of different surfaces in the emissivity table probably compensate for most of the regional discrepancies.

MODIS and ASTER emissivity libraries offer an open source of information for assigning wavelength specific emissivity values for different land surfaces. It is, however, not a straightforward process to compile the real-life CORINE class-specific emissivities based on the typically laboratory-based material-specific library entries. We have carefully considered the emissivities and their potential seasonal variations and produced a lookup table (Table 1) that serves to provide CORINE emissivity information for further use.

The method applied in the current study will allow production of spatially continuous AT datasets also in cities with few temperature observations. Together with local LST data (extracted from remotely sensed data), any seasonal regression equation in Fig. 5 can be applied as such after replacing the constant value by locally observed air temperature value, serving as a baseline for the local temperature conditions. Should there be a large number of air temperature observations available from different land uses, one can also modify the present equation to better reflect the local conditions.

This is valuable for versatile urban planning, and for a number of scientific and commercial applications. Continuous AT maps will provide an opportunity e.g., for human comfort and health based installation of green infrastructure. Mitigating the UHI hotspots with green surfaces could significantly decrease the negative impacts of climate change and urbanization (e.g., Corburn, 2009; Akbari et al., 2016).

### 8. Conclusions

The challenge in acquiring detailed temperature information in urban areas arises from the fact that remotely sensed land surface temperatures are not necessarily reliable representations of ambient air temperatures. This is clearly demonstrated in our analyses, especially for the summer season with high solar irradiance. We have developed a reasonably simple method for improving high spatial resolution temperature information using open data. The present study demonstrated that it is possible to reliably (ca. half-a-degree accuracy; MAE 0.36–0.62 °C) predict urban air temperatures (AT) at 3-m elevation using satellite remote sensing data, land cover information, and emissivity libraries. We employed Landsat 8 thermal band 10, CORINE land cover classification, and MODIS & ASTER emissivity libraries to produce AT maps at 20 m spatial resolution. Our dense reference dataset of thermometer-based AT observations allowed us to evaluate the quality of the remote sensing based predictions. However, our method allows acquiring the temperature information without this kind of detailed reference, which is typically not available in cities. CORINE-based emissivity map proved to be a well-performing way to map emissivity indirectly through open access LULC classification.

Correlation and regression analyses demonstrate that the relationship between surface and air temperature varies seasonally. Except for December, the Pearson's correlation coefficients were statistically significant (0.449–0.654,  $p \leq 0.001$ ). The modelling accuracy was best in spring, summer and autumn months. Although the explanatory power of the model was weaker in the early winter time, the ATs were still predictable with little error. The method described here can be applied in no-snow conditions only.

Through the spatially continuous AT maps, seasonal urban heat and cold islands are easily detectable. The predicted continuous air temperature clearly exhibited the dispersed nature of temperature differences in the city. Most of the high temperature hot spots were in the areas of large buildings with dark, low albedo roofs, or large asphalt surfaces such as parking lots. The relatively cool areas consisted of vegetation, or were located near water bodies, or a combination of the two, demonstrating the importance of green infrastructure as a cooling agent. Our method will support urban planning in mitigating urban heat island effect, for example in the form of tactical installation of green infrastructure in built-up areas.

### 9. Software used

Arc GIS 10.3.1, SPSS version 24 and Mendeley.

#### CRediT authorship contribution statement

**Umer Alvi:** Conceptualization, Data curation, Funding acquisition, Investigation, Methodology, Validation, Visualization, Writing – original draft, Writing – review & editing. **Juuso Suomi:** Conceptualization, Data curation, Formal analysis, Investigation,

Methodology, Supervision, Validation, Visualization, Writing – original draft, Writing – review & editing. **Jukka Käyhkö:** Conceptualization, Funding acquisition, Investigation, Methodology, Supervision, Project administration, Resources, Validation, Visualization, Writing – original draft, Writing – review & editing.

## Declaration of Competing Interest

The authors declare that they have no known competing financial interests or personal relationships that could have appeared to influence the work reported in this paper.

## Acknowledgments

We are grateful for the support from the Department of Geography and Geology, University of Turku in the form of infrastructure and finance. We thank the City of Turku for collaboration and financial support. We acknowledge the Finnish Meteorological Institute (FMI) and the United States Geological Survey (USGS) for providing the necessary data openly available for the research.

## Appendix A. Supplementary data

Supplementary data to this article can be found online at <https://doi.org/10.1016/j.ulclim.2022.101123>.

## References

- Akbari, H., Cartalis, C., Kolokotsa, D., Muscio, A., Pisello, A.L., Rossi, F., 2016. Local climate change and urban heat island mitigation techniques – the state of the art. *J. Civ. Eng. Manag.* 22 (1), 1–16. <https://doi.org/10.3846/13923730.2015.1111934>.
- Alavipanah, S., Wegmann, M., Qureshi, S., Weng, Q., Koellner, T., 2015. The role of vegetation in mitigating urban land surface temperatures: a case study of Munich, Germany during the warm season. *Sustainability (Switzerland)* 7 (4), 4689–4706. <https://doi.org/10.3390/su7044689>.
- Atmospheric Correction Parameter Calculator, 2019 (Accessed July 4, 2019), from. <https://atmcorr.gsfc.nasa.gov/>.
- Auringon nousu- ja laskujaat Suomessa, 2019 (Accessed July 4, 2019), from. <http://www.moisio.fi/taivas/aurinko.php>.
- Avdan, U., Jovanovska, G., 2016. Algorithm for automated mapping of land surface temperature using LANDSAT 8 satellite data. *J. Sens.* 1–8 <https://doi.org/10.1155/2016/1480307>.
- Azevedo, J.A., Chapman, L., Muller, C.L., 2016. Quantifying the daytime and night-time urban Heat Island in Birmingham, UK: a comparison of satellite derived land surface temperature and high resolution air temperature observations. *Remote Sens.* 8 (2).
- Barlow, J.F., 2014. Progress in observing and modelling the urban boundary layer. *Urban Clim.* 10 (P2), 216–240. <https://doi.org/10.1016/j.ulclim.2014.03.011>.
- Barsi, J.A., Barker, J.L., Schott, J.R., 2003. An Atmospheric Correction Parameter Calculator for a single thermal band earth-sensing instrument. In: IEEE International Geoscience and Remote Sensing Symposium, pp. 2–4. <https://doi.org/10.1109/IGARSS.2003.1294665>, 00(C).
- Barsi, J.A., Schott, J.R., Pallucconi, F.D., Hook, S.J., 2005. Validation of a web-based atmospheric correction tool for single thermal band instruments. *Proc. SPIE* 5882 (5882), 58820E. <https://doi.org/10.1117/12.619990>.
- Caihua, Y., Yonghong, L., Weijun, Q., Weidong, L., Cheng, L., 2011. Application of urban thermal environment monitoring based on remote sensing in Beijing. *Procedia Environ. Sci.* 11 (PART C), 1424–1433. <https://doi.org/10.1016/j.proenv.2011.12.214>.
- Chen, X.-L., Zhao, H.-M., Li, P.-X., Yin, Z.-Y., 2006. Remote sensing image-based analysis of the relationship between urban heat island and land use/cover changes. *Remote Sens. Environ.* 104 (2), 133–146. <https://doi.org/10.1016/j.rse.2005.11.016>.
- Copernicus, 2021. Land Monitoring Service, CORINE Land Cover (Accessed 23 April, 2021), from: <https://land.copernicus.eu/pan-european/corine-land-cover>.
- Corburn, J., 2009. Cities, climate change and urban heat island mitigation: localising global environmental science. *Urban Stud.* 46 (2), 413–427. <https://doi.org/10.1177/0042098008099361>.
- CORINE, 1994. CORINE land cover. *Methodology. 1–163*.
- Dos Santos, R.S., 2020. Estimating spatio-temporal air temperature in London (UK) using machine learning and earth observation satellite data. *Int. J. Appl. Earth Obs. Geoinf.* 88 (October 2018), 102066. <https://doi.org/10.1016/j.jag.2020.102066>.
- Environment, 2016. Regional land use planning (Accessed July 4, 2019), from. [https://www.ymparisto.fi/en-US/Living\\_environment\\_and\\_planning/Land\\_use\\_planning\\_system/Regional\\_land\\_use\\_planning](https://www.ymparisto.fi/en-US/Living_environment_and_planning/Land_use_planning_system/Regional_land_use_planning).
- Feizizadeh, B., Blaschke, T., 2013. Examining urban heat island relations to land use and air pollution: multiple endmember spectral mixture analysis for thermal remote sensing. *IEEE J. Select. Top. Appl. Earth Observ. Remote Sens.* 6 (3), 1749–1756. <https://doi.org/10.1109/JSTARS.2013.2263425>.
- Finnish Meteorological Institute, 2019. Seasons in Finland (Accessed July 4, 2019), from. <https://en.ilmatieteenlaitos.fi/seasons-in-finland>.
- Finnish Meteorological Institute, 2020a. Download Observations (Accessed April 18, 2020), from. <https://en.ilmatieteenlaitos.fi/download-observations#!/>.
- Finnish Meteorological Institute, 2020b. Download Observations (Accessed May 8, 2020), from. <https://en.ilmatieteenlaitos.fi/download-observations#!/>.
- Flores, P.F., Lillo, S.M., 2010. Simple air temperature estimation method from Modis satellite images on a regional scale. *Chil. J. Agric. Res.* 70 (3), 436–445. Retrieved from. [http://www.scielo.cl/scielo.php?pid=S0718-58392010000300011&script=sci\\_abstract&lng=pt](http://www.scielo.cl/scielo.php?pid=S0718-58392010000300011&script=sci_abstract&lng=pt).
- Gallo, K.P., Owen, T.W., 1998. Assessment of urban heat islands: a multi-sensor perspective for the Dallas-Ft. worth, USA region. *Geocarto Int.* 13 (4), 35–41. <https://doi.org/10.1080/10106049809354662>.
- Georgiou, A.M., Akçit, N., 2017. Comparison of MODIS-derived Land Surface Temperature with Air Temperature Measurements (September), p. 55. <https://doi.org/10.1117/12.2279339>.
- Grimm, Nancy B., Faeth, Stanley H., Golubiewski, Nancy E., Redman, Charles L., Bai, Xuemei, Briggs, John M., Faeth, S.H., Redman, C.L., Wu, J., Bai, X., Briggs, J., Golubiewski, N.E., 2008. Global change and the ecology of cities. *Science* 319 (5864), 756–760.
- Härmä, P., Hatunen, Törmä, N., Järvenpää, E., Kallio, M., Teiniranta, R., Kiiski, T., Suikkanen, J., 2015. Corine 2012 Final Report Finland GIO Land Monitoring 2011–2013 in the Framework of Regulation (EU) No 911/2010 - Pan-EU Component - Grant Agreement 3541/B2012/R0-GIO/EEA.55037.
- Harun, Z., Reda, E., Abdulrazzaq, A., Abbas, A.A., Yusup, Y., Zaki, S.A., 2020. Urban heat island in the modern tropical Kuala Lumpur: comparative weight of the different parameters. *Alexandria Eng. J.* 59, 4475–4489. <https://doi.org/10.1016/j.aej.2020.07.053>.
- Heino, E., Hellsten, E., 1991. Climatological statistics in Finland 1961–1990. In: *Meteorological Yearbook of Finland. Part 1. Ilmastohavainnot, nide 90, liite*.
- Hjort, J., Suomi, J., Käyhkö, J., 2011. Spatial prediction of urban-rural temperatures using statistical methods. *Theor. Appl. Climatol.* 106 (1–2), 139–152. <https://doi.org/10.1007/s00704-011-0425-9>.
- Hjort, J., Suomi, J., Käyhkö, J., 2016. Extreme urban-rural temperatures in the coastal city of Turku, Finland: quantification and visualization based on a generalized additive model. *Sci. Total Environ.* 569–570, 507–517. <https://doi.org/10.1016/j.scitotenv.2016.06.136>.

- Jin, M.S., 2012. Developing an index to measure urban heat island effect using satellite land skin temperature and land cover observations. *J. Clim.* 25 (18), 6193–6201. <https://doi.org/10.1175/JCLI-D-11-00509.1>.
- Käyhkö, N., Skånes, H., 2008. Retrospective land cover/land use change trajectories as drivers behind the local distribution and abundance patterns of oaks in South-Western Finland. *Landsc. Urban Plan.* 88 (1), 12–22. <https://doi.org/10.1016/j.landurbplan.2008.07.003>.
- Koskinen, J.T., Poutiainen, J., Schultz, D.M., Joffre, S., Koistinen, J., Saltikoff, E., Viisanen, Y., 2011. The Helsinki testbed: a mesoscale measurement, research, and service platform. *Bull. Am. Meteorol. Soc.* 92 (3), 325–342. <https://doi.org/10.1175/2010BAMS2878.1>.
- Lee, D., Oh, K., 2019. Developing the urban thermal environment management and planning (UTEMP) system to support urban planning and design. *Sustainability (Switzerland)* 11 (8).
- Leyre, I.E., Dobbelsteen, A.V.D., Hoeven, F.V.D., 2016. Integrating urban heat assessment in urban plans. *Sustainability (Switzerland)* 8 (4).
- Meerdink, S.K., Hook, S.J., Roberts, D.A., Abbott, E.A., 2019. The ECOSTRESS spectral library version 1.0. *Remote Sens. Environ.* 230, 111196 <https://doi.org/10.1016/j.rse.2019.05.015>.
- Mirzaei, M., Verrelst, J., Arbabi, M., Shaklabadi, Z., Lotfizadeh, M., 2020. Urban Heat Island monitoring and impacts on Citizen's general health status in Isfahan Metropolis: a remote sensing and field survey approach. *Remote Sens.* 12, no. 8, 1350. <https://doi.org/10.3390/rs12081350>.
- MODIS UCSB Emissivity Library, 1999 (Accessed July 4, 2019), from <https://icesc.eri.uscd.edu/modis/EMIS/html/em.html>.
- Monteiro, F.F., Gonçalves, W.A., Andrade, L.D.M.B., Villavicencio, L.M.M., Cássia Dos Santos Silva, C.M., 2021. Assessment of urban Heat Islands in Brazil based on MODIS remote sensing data. *Urban Clim.* 35 (October 2020).
- NASA, 2021a. Terra Instruments (Accessed April 3, 2021), from <https://terra.nasa.gov/about/terra-instruments>.
- NASA, 2021b. MODIS Land Surface Temperature and Emissivity (MOD11) (Accessed April 3, 2021, from <https://modis.gsfc.nasa.gov/data/dataproduct/mod11.php>.
- Ng, Y., 2015. A study of urban Heat Island using "local climate zones" – the case of Singapore. *Br. J. Environ. Clim. Change* 5 (2), 116–133. <https://doi.org/10.9734/BJCC/2015/13051>.
- Nichol, J.E., Pui, Hang T., 2012. Temporal characteristics of thermal satellite images for urban heat stress and Heat Island mapping. *ISPRS J. Photogramm. Remote Sens.* 74, 153–162.
- Nichol, J.E., Wong, M.S., 2008. Spatial variability of air temperature and appropriate resolution for satellite-derived air temperature estimation. *Int. J. Remote Sens.* 29 (24), 7213–7223. <https://doi.org/10.1080/0143160802192178>.
- Oke, T.R., 1976. The distinction between canopy and boundary layer urban heat islands. *Atmosphere*. 14 (July 2015), 268–277. <https://doi.org/10.1080/00046973.1976.9648422>.
- Oke, T.R., 1987. *Boundary Layer Climates (2nd Edito)*. Routledge, London and New York.
- Oke, T.R., 1995. Wind Climate in Cities. <https://doi.org/10.1007/978-94-017-3686-2>.
- Overeem, A., Robinson, J.C.R., Leijnse, H., Steeneveld, G.J., Horn, B.K.P., Uijlenhoet, R., 2013. Crowdsourcing urban air temperatures from smartphone battery temperatures. *Geophys. Res. Lett.* 40 (15), 4081–4085. <https://doi.org/10.1002/grl.50786>.
- Peel, M.C., Finlayson, B.L., McMahon, T.A., 2007. Updated world map of the Köppen-Geiger climate classification. *Hydrol. Earth Syst. Sci. Discuss.* 4 (2), 439–473. <https://doi.org/10.5194/hessd-4-439-2007>.
- Pichierri, M., Bonafoni, S., Biondi, R., 2012. Satellite air temperature estimation for monitoring the canopy layer heat island of Milan. *Remote Sens. Environ.* 127, 130–138. <https://doi.org/10.1016/j.rse.2012.08.025>.
- Pirinen, P., Simola, H., Aalto, J., Kaukoranta, J.-P., Karlsson, P., Ruuhela, R., 2012. Tilastoja suomen ilmastosta 1981-2010 (Climatological statistics of Finland 1981-2010). In Rep. 2012, 1. Retrieved from [https://helda.helsinki.fi/bitstream/handle/10138/35880/Tilastoja\\_Suomen\\_ilmostosta\\_1981\\_2010.pdf?sequence=4](https://helda.helsinki.fi/bitstream/handle/10138/35880/Tilastoja_Suomen_ilmostosta_1981_2010.pdf?sequence=4).
- Procházka, J., Brom, J., Státný, J., Pecharová, E., 2011. The impact of vegetation cover on temperature and humidity properties in the reclaimed area of a brown coal dump. *Int. J. Min. Reclam. Environ.* 25, 350–366. <https://doi.org/10.1080/17480930.2011.623830>.
- Rodríguez-Lado, L., Sparovek, G., Vidal-Torrado, P., Dourado-Neto, D., Macías-Vázquez, F., 2007. Modelling air temperature for the state of São Paulo, Brazil. *Sci. Agric.* 64 (5), 460–467. <https://doi.org/10.1590/S0103-90162007000500002>.
- Schwarz, N., Schlink, U., Franck, U., Großmann, K., 2012. Relationship of land surface and air temperatures and its implications for quantifying urban heat island indicators—an application for the city of Leipzig (Germany). *Ecol. Indic.* 18, 693–704. <https://doi.org/10.1016/j.ecolind.2012.01.001>.
- Shahmohamadi, P., Che-Ani, A.I., Etessam, I., Maulud, K.N.A., Tawil, N.M., 2011. Healthy environment: the need to mitigate urban Heat Island effects on human health. *Proc. Eng.* 20, 61–70.
- Sheng, L., Tang, X., You, H., Gu, Q., Hu, H., 2017. Comparison of the urban heat island intensity quantified by using air temperature and Landsat land surface temperature in Hangzhou, China. *Ecol. Indic.* 72, 738–746. <https://doi.org/10.1016/j.ecolind.2016.09.009>.
- Sobrino, José A., Jiménez-Muñoz, J.C., Paolini, L., 2004. Land surface temperature retrieval from LANDSAT TM 5. *Remote Sens. Environ.* 90 (4), 434–440. <https://doi.org/10.1016/j.rse.2004.02.003>.
- Sobrino, J.A., Oltra-Carrió, R., Jiménez-Muñoz, J.C., Julien, Y., Sòria, G., Franch, B., Mattar, C., 2012. Emissivity mapping over urban areas using a classification-based approach: application to the dual-use European security IR experiment (DESIREX). *Int. J. Appl. Earth Obs. Geoinf.* 18 (1), 141–147. <https://doi.org/10.1016/j.jag.2012.01.022>.
- Stathopoulou, M., Cartalis, C., 2007. Daytime urban heat islands from Landsat ETM+ and Corine land cover data: an application to major cities in Greece. *Sol. Energy* 81 (3), 358–368. <https://doi.org/10.1016/j.solener.2006.06.014>.
- Stathopoulou, M., Cartalis, C., Petrakis, M., 2007. Integrating Corine Land Cover data and Landsat TM for surface emissivity definition: application to the urban area of Athens, Greece. *Int. J. Remote Sens.* 28, 3291–3304. <https://doi.org/10.1080/01431160600993421>, 15 (July 2007).
- Streutker, D.R., 2003. Satellite-measured growth of the urban heat island of Houston, Texas. *Remote Sens. Environ.* 85 (3), 282–289. [https://doi.org/10.1016/S0034-4257\(03\)00007-5](https://doi.org/10.1016/S0034-4257(03)00007-5).
- Suomi, J., Käyhkö, J., 2012. The impact of environmental factors on urban temperature variability in the coastal city of Turku, SW Finland. *Int. J. Climatol.* 32 (3), 451–463. <https://doi.org/10.1002/joc.2277>.
- Suomi, J., Hjort, J., Käyhkö, J., 2012. Effects of scale on modelling the urban heat island in Turku, SW Finland. *Clim. Res.* 55 (2), 105–118. <https://doi.org/10.3354/cr01123>.
- The European Space Agency, 2021. Land Surface Temperature (LST) (Accessed April 3, 2021), from <https://sentinels.copernicus.eu/web/sentinel/technical-guides/sentinel-3-s3strl/level-2/land-surface-temperature-lst>.
- Tsou, Jinyeu, Zhuang, J., Li, Y., Zhang, Y., 2017. Urban Heat Island assessment using the Landsat 8 data: a case study in Shenzhen and Hong Kong. *Urban Sci.* 1 (1), 10. <http://www.mdpi.com/2413-8851/1/1/10>.
- Unger, J., Gal, T., Rakonczai, J., Mucsi, L., Szatmari, J., Tobak, Z., Leeuwen, B.V., Fiala, K., 2009. Air temperature versus surface temperature in urban environment. In: The Seventh International Conference on Urban Climate (July), pp. 3–6.
- United States Environment Protection Agency, 2021. Heat Island Impacts (Accessed April 3, 2021), from <https://www.epa.gov/heatislands/heat-island-impacts>.
- United States Geological Survey (USGS), 2017a. How does Landsat 8's 12-bit data improve data products? (Accessed May 03, 2017), from <https://landsat.usgs.gov/how-does-landsat-8s-12-bit-data-improve-data-products>.
- United States Geological Survey (USGS), 2019. How does Landsat 8 differ from previous Landsat satellites? (Accessed May 05, 2017), from <https://landsat.usgs.gov/how-does-landsat-8-differ-previous-landsat-satellites>.
- United States Geological Survey (USGS), 2019. Landsat Missions.Using the USGS Landsat Level-1 Data Product (Accessed July 4, 2019), from <https://www.usgs.gov/land-resources/nli/landsat/using-usgs-landsat-level-1-data-product>.
- United States Geological Survey (USGS), 2021a. Landsat 8 (Accessed April 3, 2021), from [https://www.usgs.gov/core-science-systems/nli/landsat/landsat-8/qt-science\\_support\\_page\\_related\\_con=0#qt-science\\_support\\_page\\_related\\_con](https://www.usgs.gov/core-science-systems/nli/landsat/landsat-8/qt-science_support_page_related_con=0#qt-science_support_page_related_con).
- United States Geological Survey (USGS), 2021b. Aster Overview. Retrieved 8 July, 2021 from <https://lpdaac.usgs.gov/data/get-started-data/collection-overview/missions/aster-overview/>.

- Voogt, J.A., Oke, T.R., 2003. Thermal remote sensing of urban climates. *Remote Sens. Environ.* 86 (3), 370–384. [https://doi.org/10.1016/S0034-4257\(03\)00079-8](https://doi.org/10.1016/S0034-4257(03)00079-8).
- Yang, Y.Z., Cai, W.H., Yang, J., 2017. Evaluation of MODIS land surface temperature data to estimate near-surface air temperature in Northeast China. *Remote Sens.* 9 (5), 1–19. <https://doi.org/10.3390/rs9050410>.
- Zaki, S.A., Othman, N.E., Syahidah, S.W., Yakub, F., Muhammad-Sukki, F., Ardila-Rey, J.A., Shahidan, M.F., Saudi, A.S.M., 2020. Effects of urban morphology on microclimate parameters in an urban university campus. *Sustain.* 12, 1–17. <https://doi.org/10.3390/su12072962>.